Water Resources Research

RESEARCH ARTICLE
10.1029/2022WR033095

Power-Function Expansion of the Polynomial Complementary Relationship of Evaporation

Jozsef Szilagyi[1,2], Ning Ma[3], Richard D. Crago[4], and Russell J. Qualls[5]

[1]Department of Hydraulic and Water Resources Engineering, Budapest University of Technology and Economics, Budapest, Hungary, [2]Conservation and Survey Division, School of Natural Resources, University of Nebraska-Lincoln, Lincoln, NE, USA, [3]Key Laboratory of Water Cycle and Related Land Surface Processes, Institute of Geographic Sciences and Natural Resources Research, Chinese Academy of Sciences, Beijing, China, [4]Department of Civil and Environmental Engineering, Bucknell University, Lewisburg, PA, USA, [5]Department of Chemical and Biological Engineering, University of Idaho, Moscow, ID, USA

Key Points:

- The power-function formulation of the nondimensional complementary relationship (CR) accounts for moisture advection
- When such admixing is negligible an existing linear version of the nondimensional CR is evoked
- Otherwise, calibration of the power-function often recaptures an existing polynomial version of the CR

Supporting Information:

Supporting Information may be found in the online version of this article.

Correspondence to:

J. Szilagyi,
szilagyi.jozsef@emk.bme.hu

Citation:

Szilagyi, J., Ma, N., Crago, R. D., & Qualls, R. J. (2022). Power-function expansion of the polynomial complementary relationship of evaporation. *Water Resources Research*, *58*, e2022WR033095. https://doi.org/10.1029/2022WR033095

Received 21 JUN 2022
Accepted 3 NOV 2022

Author Contributions:

Conceptualization: Jozsef Szilagyi
Formal analysis: Russell J. Qualls
Methodology: Jozsef Szilagyi, Ning Ma
Resources: Ning Ma
Validation: Jozsef Szilagyi
Writing – original draft: Jozsef Szilagyi
Writing – review & editing: Ning Ma, Richard D. Crago

Abstract The linear form of the nondimensional complementary relationship (CR) follows from an isenthalpic process of evaporation under a constant surface available energy and unchanging wind. Mixing of external moisture into the boundary layer (BL) alters the dry-end second-type boundary condition yielding a polynomial that can be further generalized into a three-parameter (Priestley-Taylor α, a, b) power function (PF_3), capable of responding to the level of such admixing. With the help of FLUXNET data and setting $a = 2$ for a possible recapture of the linear and/or polynomial versions of the CR, it is demonstrated that the resulting two-parameter PF (i.e., PF_2) excels among the CR-based two-parameter models considered in this study. PF_2 is then employed with a globally set constant value of $\alpha = 1.1$ and 0.5° monthly data across Australia, while calibrating b against the multiyear water-balance evaporation rate on a cell-by-cell basis. The resulting bi-modal histogram peaks first near $b = 2$ (recapturing the polynomial CR) when moisture admixing is significant, and then at $b \to 1$ (yielding the linear CR) when mixing effects are negligible. Unlike the linear or polynomial CR versions, PF_2 can respond to the general efficiency of external moisture admixing through its parameter b, making it applicable even near sudden discontinuities in surface moisture. A new duality emerges with the PF_2: while α accounts for the effect of entrainment of free tropospheric drier air into the BL on the resulting wet-environment evaporation rate, b does so for moisture on the drying-environment evaporation rates.

Plain Language Summary The power-function expansion of the polynomial complementary relationship of evaporation can account for the effect of large-scale moisture transport into the drying region thus making it more versatile in practical applications.

1. Introduction

The complementary relationship (CR) of evaporation is a powerful tool [see the latest global studies by Brutsaert et al. (2020) and Ma et al. (2021)] for predicting actual land evaporation (E) rates with the help of basic meteorological variables (i.e., air temperature, humidity, net surface radiation and wind speed) all obtained at a single elevation above the ground. Since its original formulation by Bouchet (1963) and subsequent practical early versions by Brutsaert and Stricker (1979) as well as Morton (1983), it has evolved into various forms based on different intuitive, sometimes heuristic arguments. The interest in the CR increased significantly with the publication of Brutsaert and Parlange (1998) who elegantly demonstrated why generally plummeting pan evaporation rates signify an intensification of the global hydrologic cycle. See Han and Tian (2020) for a concise overview of the relevant CR studies.

After almost six decades of the groundbreaking study by Bouchet (1963), and encouraged by the apparent success of Brutsaert and Parlange (1998) of solving even climate change issues by the CR, Szilagyi (2021) as well as Crago and Qualls (2021) engaged in finding a thermodynamic foundation for it, following the lead of Monteith (1981) who first defined the thermodynamic pathway a parcel of air near the evaporating drying surface must follow under unchanging wind conditions and constant available energy (Q_n) at the surface during an adiabatic and isobaric (i.e., isenthalpic) process. A constancy of Q_n can only be expected on the daily or longer time steps (as averaging periods) with which the CR is typically applied, although Katul and Parlange (1992) and Parlange and Katul (1992) presented guidelines for sub-daily applications as well.

Crago and Qualls (2021) and Szilagyi (2021) extended the study of Monteith (1981) by considering a full wet-to-dry cycle and simultaneously tracing the state of the air parcel at the land surface in addition to the one near to it (e.g., 2-m above ground). The key to success lies in the estimation of the wet surface temperature (T_{ws}) from measurements taken under typical, drying (i.e., not completely wet) environmental conditions for anchoring the surface isenthalp to the saturation vapor pressure curve in the state diagram.

With the help of the two isenthalps, Qualls and Crago (2020) graphically illustrated how evaporation occurs from saturated surfaces. Using a similar approach, Crago and Qualls (2021) reproduced an existing linear nondimensional formulation of the CR (Crago & Qualls, 2018), while Szilagyi (2021) independently of them and by a different approach replicated both the existing linear as well as the polynomial formulation of the CR (Szilagyi et al., 2017), the latter having been inspired by the study of Brutsaert (2015).

A critical element in Brutsaert's (2015) derivation of his polynomial CR version is the choice of the second-type boundary condition (BC) at the dry-end of the resulting nondimensional curve, effectively decoupling evaporation rates from the moisture content of the air during extreme dry conditions. His explanation of this BC, while intuitive, is not a full physical explanation of how and why this should happen, adding further stimulation for the present study, especially since the explanation resulting from it has important consequences on the applicability of the current power-function formulation of the CR.

In this study, first Szilagyi's (2021) thermodynamical approach of the CR is summarized leading to the linear as well as the polynomial nondimensional CR equations. Then the latter is expanded by a power function (PF) formulation to make it more flexible. The resulting three-parameter PF (i.e., PF_3) is simplified by fixing one of its parameters. The so-obtained two-parameter PF (i.e., PF_2) can recapture the existing linear and polynomial versions and it is applied with daily measurements of air temperature (T), pressure (p), vapor pressure deficit (VPD), net radiation (R_n), ground heat conduction (G) and wind speed (u) in addition to eddy-covariance observed (Pastorello et al., 2020) sensible (H) and latent heat (LE) fluxes for validation at seven Australian FLUXNET sites. The so-derived E values are then compared with similar estimates of three additional CR-based evaporation methods by Brutsaert (2015), Han et al. (2012), and Gao and Xu (2021), to demonstrate the predictive capability of the present PF approach. All three methods have two parameters to calibrate, similar to the present power-function (PF_2) one.

Finally, the PF_2 with its α value set to 1.1 globally by Ma et al. (2021), employing the method of Szilagyi et al. (2017), is applied with 0.25° gridded monthly input data after aggregation to 0.5° values over Australia and its sole free parameter (b) calibrated on a cell-by-cell basis against 0.5° simplified water-balance derived evaporation estimates (E_{wb}) to see how its value changes spatially and what may drive those changes.

Australia, as a testing ground was chosen because of its diverse climate from tropical to subtropical to semi-desert to Mediterranean to oceanic, resulting in a wide range of aridity values and a sudden and strong discontinuity in surface moisture conditions especially across its western shore.

Note that this work is not meant as a calibration/verification analysis of a preferred two-parameter approach over other existing similar (or single parameter) approaches. That is why the steps required for such a study (i.e., validation with data separate from calibration, sensitivity analysis of the parameters, etc.) are deliberately not repeated here, specifically because it would blur the above focus of the present work. The overarching goal of the present study is a deeper understanding of the CR obtainable from a thermodynamics-based approach and as a result the elevation of the CR status from being considered as an approach based mostly on intuitive arguments to a physically better founded one.

2. A Concise Thermodynamical Derivation of the Nondimensional Polynomial Complementary Relationship

During drying out of the environment under unchanging wind conditions, constant pressure as well as constant available energy, Q_n (= $R_n - G$) at the surface, the change in vapor pressure (e) is strictly tied to changes in air temperature (T) near the surface via the equation (Monteith, 1981; Qualls & Crago, 2020; Szilagyi, 2021)

$$de/dT = -\gamma \tag{1}$$

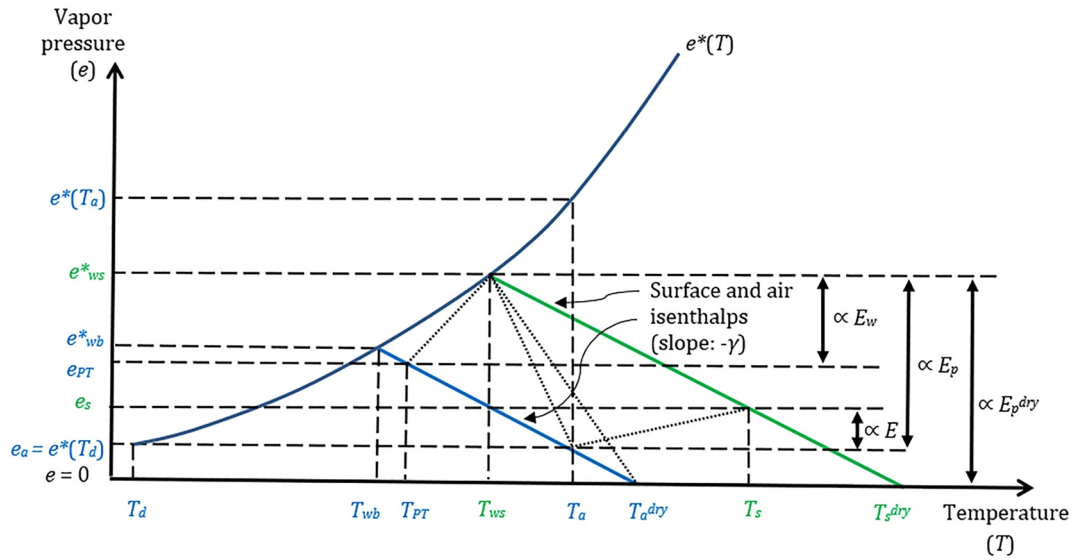

Figure 1. Saturation vapor pressure (e^*) curve, air (blue) and surface (green) isenthalps (Crago & Qualls, 2021; Szilagyi, 2021) during a full drying-out of the environment from completely wet to a completely dry state. The vertical and horizontal projections of the dotted lines are proportional ($\propto$) to the different latent ($E \le E_w \le E_p \le E_p^{dry}$) and corresponding sensible (the latter negative–directed toward to surface–for E_p and E_p^{dry}) heat fluxes. See Table 1 for definition of the different variables.

Here $\gamma = c_p p(0.622L_v)^{-1}$ is the psychrometric constant, c_p the specific heat of air under constant pressure, and L_v is the latent heat of vaporization. Equation 1 forms straight (air and surface) isenthalpic lines of slope -γ emanating from the saturation vapor pressure curve, $e^*(T)$, in the state diagram (Figure 1), provided the slight dependence of L_v on T is neglected under typical environmental conditions.

The saturation vapor pressure (hPa) can be obtained, for example, by the Teten's formula as $e^*(T) = 6.108\exp[17.27T/(237.3 + T)]$ where T is supplied in C° (Stull, 2000). The wet-bulb temperature, T_{wb}, is the lowest temperature the air at the measurement height can attain by evaporation, but this temperature is rarely reached during natural processes due to large-scale mixing of relatively dry free-tropospheric air into the convective boundary layer (Brutsaert, 1982; Lhomme, 1997). Instead, a wet-environment air temperature, $T_{PT} \ge T_{wb}$, generally occurs. Note that by placing (T_{PT}, e_{PT}) on the same isenthalp that goes through (T_a, e_a) in Figure 1, assumes that the energy import associated with such entrainment is negligible to Q_n. T_{PT} however is not known during drying conditions of the environment (i.e., when $T_a > T_{PT}$), but it can be estimated by the wet-surface temperature, T_{ws}, capped by T_a whenever $T_{ws} > T_a$. This substitution of T_{PT} with T_{ws} is possible only because in warm and humid conditions air temperature changes mildly with elevation above the ground (Laikhtman, 1964; Stull, 2000; Szilagyi, 2014). The capping is necessary since wet-environmental air temperature, T_{PT}, must always be lower than the drying one (T_a) due to evaporation cooling.

T_{ws} can be estimated (Szilagyi & Jozsa, 2008) by writing out the Bowen ratio (i.e., H/LE) for a plot-sized wet patch utilizing the Penman (1948) equation for E_p (mm d^{-1}), yielding the evaporation rate of such a small wet area, as

$$\frac{H}{LE} = \frac{Q_n - E_p}{E_p} \approx \gamma \frac{T_{ws} - T_a}{e^*(T_{ws}) - e_a} \tag{2}$$

where the small size of the wet patch means it cannot alter the temperature and humidity of the overpassing air significantly, measured upwind of it. In the right-hand-side of Equation 2 it was assumed that the eddy diffusivities for temperature and specific humidity are equal which is only approximate for advective conditions (Assouline et al., 2008) described by Equation 2. Note that E specified in water depth can be transformed into energy flux (LE) values by $LE = L_v\rho_w E$, and vice-versa for Q_n, where ρ_w is the density of water. Equation 2 is implicit for T_{ws}, requiring iterations to solve.

The Penman equation (applicable on a time scale of a day or longer) is given by

$$E_p = \frac{\Delta Q_n}{\Delta + \gamma} + \frac{\gamma f_u [e^*(T_a) - e_a]}{\Delta + \gamma} \quad (3)$$

where Δ denotes the slope of the saturation vapor pressure curve (hPa $C^{\circ -1}$) at the measured air temperature, T_a, and the empirical wind function, f_u (mm d^{-1} hPa^{-1}), is traditionally specified as $f_u = 0.26(1 + 0.54u_2)$ (Brutsaert, 1982). Here u_2 (m s^{-1}) is the horizontal wind speed at 2-m above the ground and can be estimated by a power function (Brutsaert, 1982) from measurements (u_h) at h m above the surface as $u_2 = u_h\,(2/h)^{1/7}$. The $e^*(T_a) - e_a$ expression in the aerodynamic term of Equation 3 is the *VPD*.

With the two isenthalps anchored to the saturation vapor pressure curve, one may notice that during a full wet-to-dry transition of the environment the (T_a, e_a) state-coordinates of Figure 1 traverse the ($T_{PT} - T_a^{dry}$, $e_{PT} - 0$), while the corresponding (T_s, e_s) coordinates track the full length of the ($T_{ws} - T_s^{dry}$, $e^*_{ws} - 0$) distance on the surface isenthalp. From the two different distances traveled during the same amount of time, two different average speed values result for the movement of the respective state coordinates. By assuming that the ratio of distances traveled on the two isenthalps during any time interval equals the constant ratio of the two average speed values, a geometric similarity emerges (Szilagyi, 2021; cf. Crago & Qualls, 2021, who used somewhat different reasoning), namely

$$\frac{e_a}{e_{PT}} = \frac{e_s}{e^*_{ws}}. \quad (4)$$

While keeping the right-hand-side of Equation 4, the left-hand-side can be augmented to

$$\frac{e_a}{e_{PT}} = \frac{e^*_{ws} - (e^*_{ws} - e_a)}{e^*_{ws} - (e^*_{ws} - e_{PT})} = \frac{e_s}{e^*_{ws}}. \quad (5)$$

The right-hand-side of Equation 5 can also be expanded into

$$\frac{e_s}{e^*_{ws}} = \frac{e_s\left(1 - \frac{e_a}{e_s}\right)}{e^*_{ws}\left(1 - \frac{e_a}{e_s}\right)} = \frac{e_s\left(1 - \frac{e_{PT}}{e^*_{ws}}\right)}{e^*_{ws}\left(1 - \frac{e_{PT}}{e^*_{ws}}\right)} = \frac{e_s - \frac{e_s}{e^*_{ws}} e_{PT}}{e^*_{ws} - e_{PT}} = \frac{e_s - e_a}{e^*_{ws} - e_{PT}}. \quad (6)$$

The combination of Equations 5 and 6 yields (Szilagyi, 2021)

$$\frac{e_s - e_a}{e^*_{ws} - e_{PT}} = \frac{e^*_{ws} - (e^*_{ws} - e_a)}{e^*_{ws} - (e^*_{ws} - e_{PT})} \quad (7)$$

which via the corresponding evaporation terms in Figure 1 can be written as

$$\frac{E}{E_w} = \frac{E_p^{dry} - E_p}{E_p^{dry} - E_w} \quad (8)$$

due to the Dalton-type formulation of any evaporation term as $E = -K\,de/dz = K_z\,(e_s - e_a)$ where K is the eddy diffusivity, z is vertical distance and K_z is K divided by the measurement height.

In Equation 8, E_p^{dry} can be obtained by Equation 3 with the $e_a = 0$ substitution, and e^* and Δ evaluated at the dry-environment air temperature, T_{dry} ($= T_a + e_a/\gamma$) (Szilagyi, 2021). The wet-environment evaporation rate, E_w, can be found from the Priestley-Taylor (1972) equation as

$$E_w = \alpha \frac{\Delta(T_{PT})\,Q_n}{\Delta(T_{PT}) + \gamma}. \quad (9)$$

The spatially and temporally constant value of the Priestley-Taylor (PT) coefficient, α, can be set without any calibration with gridded data, covering a large spatial domain and thus ensuring the presence of permanently or periodically wet areas, by the method of Szilagyi et al. (2017), otherwise, it must be calibrated, typically within the [1–1.32] interval (Morton, 1983). The PT-α corrects for the evaporation enhancing effect of drier free-atmospheric air admixing (Lhomme, 1997) into the daytime growing convective boundary layer (BL) by its larger than unity value. It also indicates that perfect adiabatic conditions on a temporal scale of a day or longer

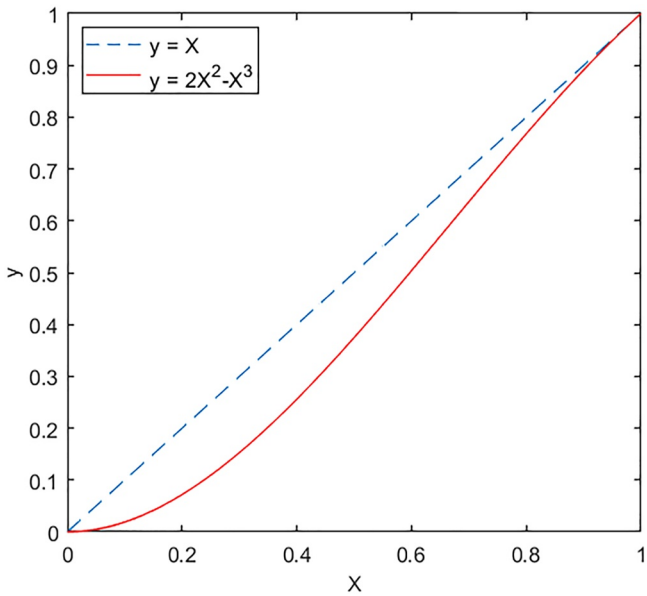

Figure 2. The linear and polynomial CR relationships between $y = E\,E_p^{-1}$ and $X = w_i\,E_w\,E_p^{-1}$.

may not generally exist as such mixing must frequently develop. Although Priestley and Taylor (1972) considered α to be a global constant, there have been numerous attempts (e.g., deBruin, 1982; McNaughton, 1976; McNaughton & Spriggs, 1989) to link the value of α to different environmental drivers, from which air temperature seems to be a strong one (Eichinger et al., 1996), yet with considerable internal variability globally (Andreas et al., 2013; Szilagyi et al., 2014).

After division by E_p, Equation 8 can be rearranged (Crago & Qualls, 2018; Szilagyi et al., 2017) into

$$y = X; \quad y \equiv \frac{E}{E_p},\ X \equiv w_i \frac{E_w}{E_p},\ w_i \equiv \frac{E_p^{dry} - E_p}{E_p^{dry} - E_w} \tag{10}$$

which is a linear relationship between the two nondimensional variables y and X. Notice that w_i acts as a wetness index, with $w_i \approx 0$ for hyper arid and $w_i = 1$ for wet conditions (Szilagyi et al., 2017). Note also that the two nondimensional variables were already obtained by Szilagyi et al. (2017) in a different way, before the present thermodynamics-based derivation was introduced. The complementarity in the CR means that E and E_p change in opposite ways (Bouchet, 1963), best seen in Equation 10 between E and E_pX. When E_p increases (i.e., the environment dries), w_i decreases while E_w remains unchanged, yielding a decreased E rate.

As an area dries, on the other hand, it evokes another effect: admixing of moisture from the surrounding larger region may occur via entrainment of relatively moist, free-tropospheric air into the drier BL and/or by direct horizontal advection of moist air. The latter process may be more localized, typical for areas lying downwind of a sea, or other large body of wet surfaces such as lakes, swamps, wetlands, but may also exist between different land cover types, such as forests and any vegetation with a much shallower root-zone (therefore in a drier state). The resulting influx of external humid air and the subsequent vertical mixing then suppress the vertical humidity gradient that would otherwise exist over the drying surface, the effect being potentially stronger the drier the surface, eventually leading to a possible complete elimination of the already weak vertical humidity gradient.

Let us consider what happens when the area has dried out completely, that is, $E = e_a = e_s = w_i = 0$ is achieved. The relative changes (dy vs. dX) in y and X of Equation 10 can then be written as: $dy = d(E/E_p) = dE/E_p - E\,dE_p/E_p^{\,2}$. The second term is zero as $E = 0$, thus $dy = (de_s - de_a)/E_p$, since $E = e_s - e_a$ from Figure 1. The corresponding change in X with the help of Equation 7 can be written as: $dX = d[(e_a\,E_w)/(e_{PT}\,E_p)] = E_w/e_{PT}\,d(e_d/E_p) = E_w/e_{PT}\,de_d/E_p$. Note that E_w and e_{PT} are conservative (invariant) quantities under isenthalpic processes. The relative change in the two dimensionless variables, y and X at $X = 0$ this way becomes: $dy/dX = [(de_s - de_a)/de_a]\,e_{PT}/E_w = [(e_s - e_a)/e_a]\,e_{PT}/E_w$ (Szilagyi, 2021). As seen, the dy/dX term vanishes when e_s is about the same as e_a. But this is exactly what can be expected due to external humidity advection over the extremely dry area with its subsequent full vertical mixing within the convective boundary layer: a (near) constant humidity profile, as the main source of this profile is not the surface moisture but rather the imported external moisture.

By considering this moisture admixing, a new relationship between y and X develops satisfying the same BCs as the linear solution, Eq. 10, with the only change for the second-type BC at $X = 0$. The four BCs (after Brutsaert, 2015) thus become i) $y = 1\,|X = 1$; ii) $dy\,/\,dX = 1\,|X = 1$, iii) $y = 0\,|X = 0$; iv) $dy\,/\,dX = 0\,|X = 0$. By seeking a polynomial solution (Turbiner, 1992), the following nondimensional CR is obtained (Szilagyi et al., 2017; Szilagyi, 2021).

$$y = 2X^2 - X^3 \tag{11}$$

Note that when admixing of moisture is negligible then the last BC is absent, allowing for the above-derived linear form, Equation 10, of the CR, obtainable without any BC considerations. Figure 2 depicts the two solutions.

If mixing of external moisture into the BL affects the shape of the CR curve during drying conditions as seen in Figure 2, one may rightly ask what effect a similar admixing of relatively dry external air does on the CR

curve during wet conditions. On the scaled variables it does not have any effect as at $X = 1$, w_i is also unity since $E_p = E_w$, therefore y stays unity even though the corresponding E value is increased by the same amount as E_w itself.

Comparison of the polynomial curve with the linear solution in Figure 2 shows that for the same value of X the corresponding scaled evaporation rate, y, is smaller than under negligible moisture influx conditions. How can one interpret the polynomial curve? What physical processes can explain its behavior?

For an answer let's start from a fully wet condition (i.e., $X = 1$) at the land surface and assume a steady supply of air with a constant specific humidity via (a) horizontal advection, and/or; (b) large-scale entrainment of free-tropospheric air, into the developing BL. This relatively drier (and potentially warmer) air enhances the wet-environment evaporation rate (E_w) before drying commences (accounted for in the larger than unity value of the PT-α), as discussed above. As the temporarily wet land starts to dry, it does not experience any significant moisture influx by the initial admixing of drier air, so the polynomial curve overlaps the linear one near $X = 1$ in Figure 2. Once the moisture content of the BL over the drying land drops below that of the external air, the polynomial curve's slope starts to increase which means that the scaled evaporation rate, y, is decreasing faster than X, as the dropping moisture content of the BL over the drying land is being replenished to some degree by the external moisture. The effect of the external moisture supply into and the subsequent mixing within the BL is not very effective in the beginning as the difference in moisture content is small yet, but it gets stronger with drying and reaches its maximum effect at $X = 2/3$ where the slope of the curve attains its maximum value of 4/3 designating a maximum deviation in behavior from isenthalpic conditions. With surface evaporation further decreasing, however, the temperature of the land continues to increase leading to more intense mixing within the day-time growing BL which gets ever thicker with the land-temperature increase thus able to "dilute" the incoming moisture ever more efficiently. As a result, the change in X to a unit drop in y starts to approach the unity rate of the isenthalpic process and attains it at $X = 1/3$ in order to further drop to zero when $X \to 0$. Note that by the time $X = 1/3$ is reached, the land/air temperature over the drying land becomes higher than it were for the negligible moisture influx case of the linear solution as the polynomial curve stays always below the linear one representing less efficient cooling of the surface by suppressed evaporation, thus making it possible to dilute the incoming moisture at a higher efficiency, reflected in the milder than unity slope for $X < 1/3$. However, there exists a physical limit (in the form of a capping inversion layer) beyond which the BL cannot grow during the day, which then also sets a limit on diluting the incoming moisture, manifested by the minimum value below which X cannot drop in reality. It may be a value (X_{min}) of 0.03 in Figure 2. Then, the $X < X_{min}$ part of the curve can only be reached when the moisture influx to the BL itself weakens and drops to zero at some point of the drying of the environment, allowing X to reach zero. The $0 < X \leq X_{min}$ interval where the slope of the polynomial curve is close to zero and this way differs most from unity marks a maximum state of decoupling of the BL moisture content from that of the underlying surface.

Equation 11 has already been applied on a monthly basis in a calibration-free mode, employing a spatially and temporally constant PT-α value with great success (outperforming mainstream complex, data-intensive evaporation models) over the United States (Ma et al., 2020; Ma & Szilagyi, 2019; Szilagyi et al., 2017), China (Ma et al., 2019), and the globe (Ma et al., 2021), while Kim et al. (2019) employed it very efficiently for historical drought assessment, also over the United States (Table 1).

3. Expansion of the Polynomial Complementary Relationship by a Power Function Approach

The application of polynomials for finding solutions to differential equations and/or (in our case) boundary value problems comes from practicality rather than mathematical necessity (Turbiner, 1992). Therefore, additional solutions to the four BCs were sought that would generalize the polynomial solution of Equation 11, meaning that Equation 11 should emerge as a special (i.e., one of the many solutions possible) case.

The polynomial in Equation 11 can be expanded by a power-function (PF) approach using the same BCs. The resulting three-parameter function (PF_3)

$$y = aX^b - (a-1)X^{\frac{ab-1}{a-1}} \quad a, b > 1 \tag{12}$$

Table 1
List of the Different Evaporation (E) Rates Employed in the Study Together With the Relevant Temperature (T) and Vapor Pressure (e) Terms Defined

E, LE	Actual evaporation, latent-heat rate
E_p	Potential (Penman) evaporation rate
E_p^{dry}	Dry-environment potential evaporation rate
E_w	Wet-environment (Priestley-Taylor) evaporation rate
T_a, e_a [$= e^*(T_d)$]	Actual air temperature, vapor pressure, saturation vapor pressure at T_d
T_a^{dry}	Dry-environment air temperature
T_d	Dew-point temperature
T_{PT}, e_{PT}	Wet-environment air temperature, vapor pressure
T_{wb}, e^*_{wb}	Wet-bulb temperature, saturation vapor pressure at T_{wb}
T_s, e_s	Actual land-surface temperature, vapor pressure
T_s^{dry}	Dry-environment land surface temperature
T_{ws}, e^*_{ws}	Wet surface temperature (Szilagyi & Jozsa, 2008), saturation vapor pressure at T_{ws}

has two parameters, a and b, additional to Equation 11. Note that by the $a = b = 2$ choice, Equation 12 transforms back into Equation 11. Figure 3 displays the ensuing curves for selected values of a and b. With the value of b increasing (from 1.4 to 2 to 3), the curves move to the right, forming three groups of curves with the a and b values picked for demonstration. Within each group the curves move upward with increasing values of a. For example, the lowest (i.e., right-most) curve has $a = 1.1$ and $b = 3$, while the one just above it belongs to $a = 1.2$, $b = 3$. For most practical applications the parameter ranges can be narrowed to $1 < a \leq 2$ and $1 < b < 10$. In Figure 3 the role of a can be viewed as fine tuning the curves for a given b value, but the opposite is also true, so the two parameters play largely similar roles.

In order to reduce the number of parameters in Equation 12 to just two (the PT-α, and b) for a meaningful comparison with other existing two-parameter CR-based methods, $a = 2$ is prescribed in this study for evaporation estimation. It transforms the PF_3 of Equation 12 into PF_2

$$y = 2X^b - X^{2b-1} \quad b > 1 \tag{13}$$

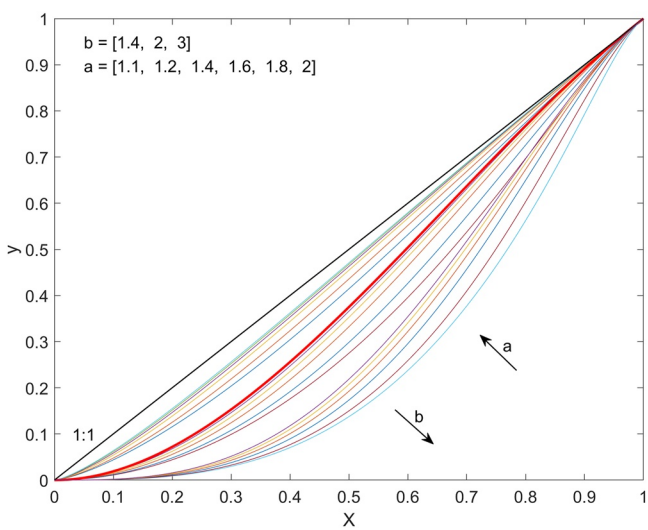

Figure 3. Graphical representation of Equation 12 (PF_3) for selected values of a and (b) The polynomial of Equation 11 ($a = b = 2$) is the heavier red line. The arrows indicate the general shifting direction of the curves to growing values of the specified parameter.

and also makes it possible that the PF curve revert to the linear expression of Equation 10 or the polynomial of Equation 11 during calibration when necessary. Figure 4 displays the resulting curves for $1 < b \leq 10$. The curve with $b = 1.001$ indeed has a vanishing slope at $X = 0$, as BC (d) requires, but it is indistinguishable from the $y = X$ line of Equation 10 by the naked eye. For this reason, during calibration of b in the ensuing analysis, a value of $b = 1$ will be allowed for practicality, even though it violates BC (d).

As seen in Figure 4, increasing values of b in PF_2 account for increasing influence of external moisture transport into the drying area, expressed by steeper slopes and wider intervals of X where $y \approx 0$. When b is close to unity, such transport is negligible and the pure isenthalpic solution (Equation 10) is approached. Cases with $b > 3$, typically signify strong horizontal advection of moisture from extensive wet surfaces (as the gridded data illustrates below for Australia). Values of $1 < b < 3$ can be expected to correspond to typical cases of external moisture influence over the drying regional surface, with or without direct horizontal advection of moisture from a nearby wet surface of regional extent.

For a further, more numerical demonstration of the effect of moisture advection on the resulting evaporation rates and the general extent of the nondimensional curve, a time-varying moisture disturbance (e') is prescribed in the form of $e' = c\,(e_s - e_a)^{1.28} VPD^{1.5}$ (where $c = 0.0011$ with a dimension neces-

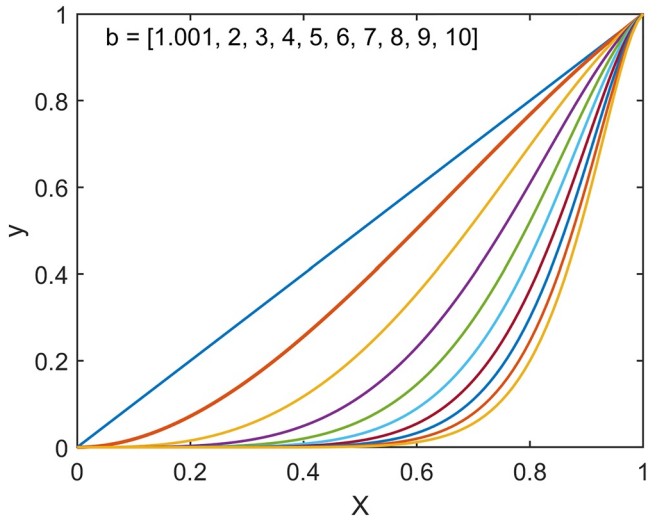

Figure 4. Graphical representation of Equation 13 (PF_2) for $1 < b \leq 10$. The polynomial of Equation 11 ($b = 2$) is the heavier red line.

sary for yielding e' in hPa), additive to the isenthalpic e_a values. Figure 5a displays the undisturbed (i.e., no advection) and disturbed (i.e., advection) e_a values during a complete drying out of the environment from an assumed fully saturated ($T_a = T_{wb}$ for simplicity) to a completely dry state ($e_a = 0$ at T_a^{dry}) with the corresponding relative humidity values. The prescribed disturbance is mild, reaching a maximum value less than 0.7 hPa (Figure 5b) as advection-produced vapor pressure enrichment, yet it can exert a considerable suppression of the evaporation rates (Figure 5c) producing a relative difference of almost 100% when the environment becomes extremely dry and the disturbed evaporation rate approaches zero. The resulting nondimensional curve is similar in overall extent to a PF_2 curve with $b = 1.4$ (Figure 5d), indeed representing a mild case of moisture advection, discussed before.

From this simulation it is evident that even a relatively small increase in the vapor pressure values due to external moisture admixing can have a considerable effect on the resulting evaporation rates.

4. Testing the Power-Function Approach With Eddy-Covariance Data

The polynomial (Equation 11) as well as the power-function (PF_2) formulations of the CR are tested with eddy-covariance data of seven Australian FLUXNET sites (Pastorello et al., 2020), displayed in Figure 6. These sites include land covers of grass, permanent wetland, open shrubland, woody savanna, and evergreen broadleaf forests. See Table S1 in Supporting

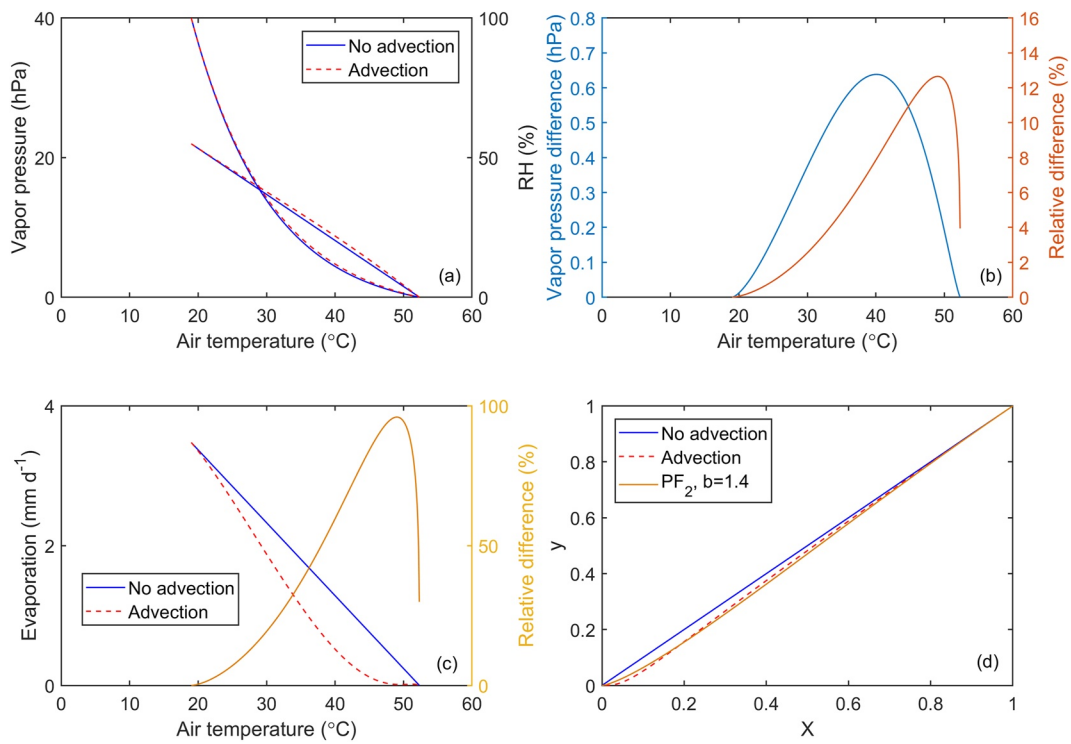

Figure 5. The simulated effect of a prescribed external moisture advection on isenthalpic evaporation during a complete drying out of the environment. Input data is from Szilagyi (2014), indicating typical warm summer conditions at mid-latitudes: $Q_n = 143$ W m^{-2} (= 5.6 mm d^{-1}), $T_{wb} = 19$°C, $T_{ws} = 21$°C, and u_2 taken as 5 m s^{-1}. (a) Air temperature varies between T_{wb} and T_a^{dry} (=52.3°C). Isenthalpic vapor pressure, e_a, is disturbed by an additive process, representing a temporally varying mild advection. Relative humidity (RH) varies between 0% and 100%. (b) Vapor pressure differences between the pure isenthalpic (no advection) and disturbed (advection) cases. (c) Resulting evaporation rates. (d) The corresponding nondimensional evaporation rates (y) as a function of X with the PF_2 ($b = 1.4$) also displayed for a comparison.

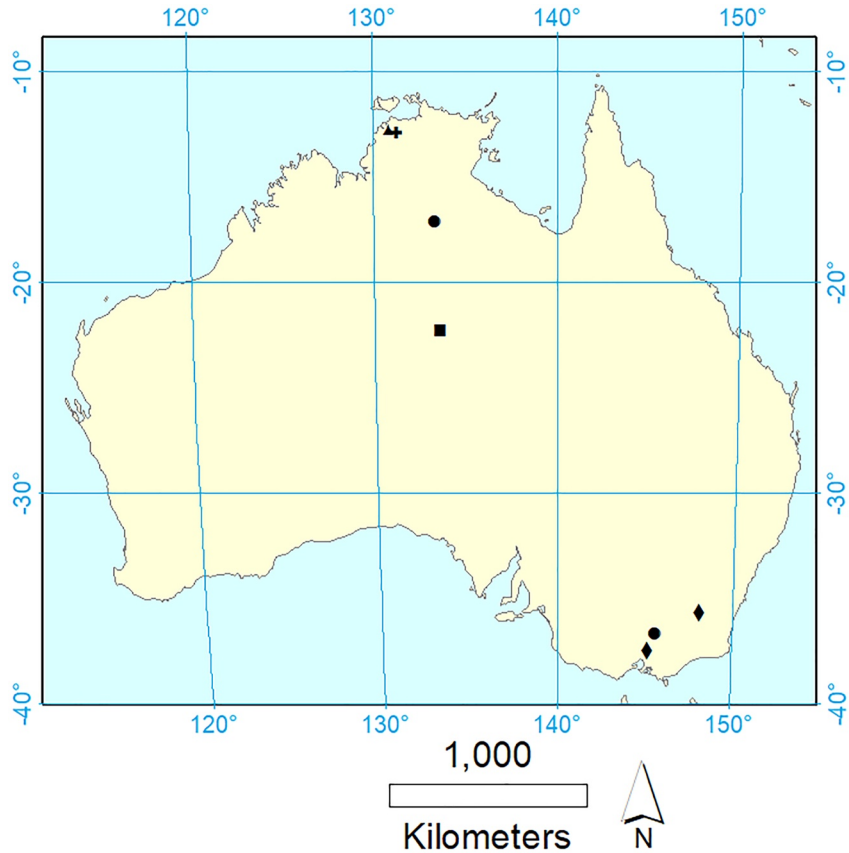

Figure 6. Location of the seven FLUXNET sites (see Table 4 for exact coordinates) with at least 1 year of daily meteorological and eddy-covariance derived flux measurements. +: permanent wetland; ▲: woody savanna; ■: open shrubland; ●: grassland; ♦: evergreen broadleaf forest.

Information S1 for information on the measurements, including site names, geographic coordinates, and periods of record. In the ensuing modeling, measurement heights for wind speed are reduced by the average height of the vegetation. The daily eddy-covariance-measured LE fluxes are Bowen-ratio corrected [i.e., $LE_c = Q_n/(1 + H\,LE^{-1})$] to close the energy budget (Twine et al., 2000), and the temperature values are converted to potential temperatures, $T_p = T_a + gz_m/c_p$, where z_m is the measurement height for air temperature, and g is the gravitational acceleration (e.g., Stull, 2000) due to the relatively large scatter in z_m among the sites (from 2.5 m for grass to 70 m for the forests). Note that in theory, T_p must replace T_a in the preceding equations (as sensible heat fluxes are driven by vertical gradients of T_p and not T_a), but the difference between them is negligible for measurement heights not far from the ground in comparison to the observed vertical change in T_a.

The evaporation estimates of Equations 11 and 13 (PF_2), employing daily, 5- and 30-day aggregated input data are compared to similar estimates of three additional two-parameter CR-based models by Brutsaert (2015), Han et al. (2012), and Gao and Xu (2021), to be referred to as B15, HT12, and GX21, respectively. In all three models and in PF_2, the two tunable parameters include the PT-α and an additional parameter (Table 2) for a meaningful comparison of the CR models. The exact representation of HT12 is chosen specifically for such a purpose of a shared PT-α.

Table 2 summarizes the three models. B15 and HT12 evaluate Equation 9 at the drying air temperature, T_a, while GX21 adopts the approach of Szilagyi and Jozsa (2008) for estimating T_{ws} and thus T_{PT} (Szilagyi, 2014). For additional information of the models, please, refer to the relevant publications.

A 5-day aggregation instead of a weekly one is chosen, because Morton (1983) argues that it is the shortest time-interval over which any effect of passing weather systems, temporarily upsetting the dynamic equilibrium between the surface and the overlying air, can be expected to be substantially subdued.

Table 2
Summary of the Three Additional Two-Parameter CR-Based Models Employed in This Study

B15	HT12[a]	GX21
$y = (2 - c)\,x^2 - (1 - 2c)\,x^3 - cx^4$	$y = [1 + k\,(x^{-1} - 1)^n\,]^{-1}$	$y = \exp[(1 - x^{-d})d^{-1}]$
$x_{B15} = E_w(T_a)\,E_p^{-1}$	$x_{HT} = \alpha^{-1}\,E_w(T_a)\,E_p^{-1}$	$x = E_w\,E_p^{-1}$
	$x_h = (0.5 + c_{HT}^{-1})[\alpha(1 + c_{HT}^{-1})]^{-1}$	
	$n = 4\alpha(1 + c_{HT}^{-1})\,x_h\,(1 - x_h)$	
	$k = [x_h\,(1 - x_h)^{-1}]^n$	
Parameters: α, c	Parameters: α, c_{HT}	Parameters: α, d

[a]Written in the form specified in Han and Tian (2018).

Performance of the calibrated models is summarized in Table 3. The four (plus Equation 11) models behave similarly in terms of the root-mean-square error (RMSE), but PF_2 produces the best results in seven out of the nine cases considered, followed by Equation 11 (four occasions, provided Equation 13 is excluded) and B15 (twice). In fact, PF_2 is always the best performing model with 30-day aggregated data. In B15 the calibrated values of the PT-α occasionally drop below the physically meaningful unity value while it is almost the norm for GX21. Interestingly, the best-fit-line slope deviates from its optimal value of unity the least with Equation 11.

Figure 7 demonstrates the increasing effect of large-scale moisture transport on the shape of the nondimensional CR curve of PF_2, as aridity progresses. For the evergreen broadleaved forests serious aridity never occurs as the majority of the points are situated at $X > 0.5$ (Figure 7b), with corresponding evaporation rates, $E_{EC} > 1$ mm d^{-1} (Figure 7a), therefore the effect of any possible horizontal moisture transport toward these sites remains negligible. As a result, calibration of PF_2 yields $b \to 1$ and thus the straight line of Equation 10 (red line in Figure 7b, on top of the 1:1 line). More serious aridity, on the other hand, can develop over the grass sites resulting in several points at $X < 0.2$ (Figure 7d), and $E_{EC} < 0.5$ mm d^{-1} (Figure 7c). Any moisture transport to the grass sites drier than their surroundings will affect the eddy-covariance measurements less than it depresses the value of E_p since

Table 3
Root-Mean-Square Error (RMSE) Values (in mm d^{-1} for Easier Comparison Among Aggregation Periods) of the CR-Based Two-, and Single-Parameter (Equation 11) Evaporation Estimation Methods at Different Australian FLUXNET Sites Displayed in Figure 6

Station/aggregation	PF_2 (Equation 13)	Equation 11	B15	HT12	GX21
All (seven sites) Daily	**0.81** $\alpha = 1.11$, $b = 1.3$ $m = 0.83$	0.89 $\alpha = 1.16$ $m = 0.94$	0.86 $\alpha = 1.05$, $c = 2.7$ $m = 0.86$	0.84 $\alpha = 1.09$, $c_{HT} = 1.3$ $m = 0.86$	0.86 $\alpha = 0.93$, $d = 1.07$ $m = 0.85$
5-day	**0.66** $\alpha = 1.13$, $b = 1.45$ $m = 0.87$	0.72 $\alpha = 1.17$ $m = 0.96$	0.7 $\alpha = 1.08$, $c = 3.3$ $m = 0.92$	0.7 $\alpha = 1.13$, $c_{HT} = 1.1$ $m = 0.91$	0.71 $\alpha = 0.97$, $d = 1.35$ $m = 0.9$
30-day	**0.51** $\alpha = 1.14$, $b = 1.55$ $m = 0.91$	**0.56** $\alpha = 1.17$ $m = 1$	0.58 $\alpha = 1.09$, $c = 3.3$ $m = 0.95$	0.59 $\alpha = 1.14$, $c_{HT} = 1.1$ $m = 0.94$	0.59 $\alpha = 0.98$, $d = 1.38$ $m = 0.93$
Grass (two sites) Daily	**0.7** $\alpha = 1.12$, $b = 1.65$ $m = 0.75$	**0.72** $\alpha = 1.18$ $m = 0.83$	0.76 $\alpha = 1.06$, $c = 3.3$ $m = 0.73$	0.75 $\alpha = 1.15$, $c_{HT} = 0.9$ $m = 0.75$	0.75 $\alpha = 0.96$, $d = 1.46$ $m = 0.74$
5-day	**0.55** $\alpha = 1.16$, $b = 1.75$ $m = 0.83$	**0.57** $\alpha = 1.21$ $m = 0.9$	0.62 $\alpha = 1.1$, $c = 3.7$ $m = 0.81$	0.61 $\alpha = 1.18$, $c_{HT} = 0.9$ $m = 0.81$	0.6 $\alpha = 1.02$, $d = 1.73$ $m = 0.84$
30-day	**0.37** $\alpha = 1.21$, $b = 1.85$ $m = 0.93$	**0.38** $\alpha = 1.24$ $m = 0.98$	0.49 $\alpha = 1.13$, $c = 3.8$ $m = 0.88$	0.48 $\alpha = 1.24$, $c_{HT} = 0.8$ $m = 0.93$	0.46 $\alpha = 1.05$, $d = 1.81$ $m = 0.92$
Forest (two sites) Daily	0.75 $\alpha = 1.11$, $b = 1$ $m = 0.93$	0.92 $\alpha = 1.15$ $m = 0.98$	**0.65** $\alpha = 0.9$, $c = -2$ $m = 0.95$	0.67 $\alpha = 1$, $c_{HT} = 5$ $m = 1$	0.7 $\alpha = 0.86$, $d = 0.1$ $m = 0.96$
5-day	0.55 $\alpha = 1.12$, $b = 1$ $m = 0.94$	0.66 $\alpha = 1.16$ $m = 1$	**0.52** $\alpha = 0.97$, $c = -0.7$ $m = 0.98$	0.53 $\alpha = 1$, $c_{HT} = 4.4$ $m = 1$	0.55 $\alpha = 0.88$, $d = 0.1$ $m = 0.98$
30-day	**0.4** $\alpha = 1.13$, $b = 1$ $m = 0.98$	0.48 $\alpha = 1.17$ $m = 1.06$	0.42 $\alpha = 0.99$, $c = -0.4$ $m = 1$	0.41 $\alpha = 1$, $c_{HT} = 5$ $m = 1.01$	0.43 $\alpha = 0.89$, $d = 0.1$ $m = 0.99$

Note. The trial-and-error-calibrated parameter values of the different methods are also displayed, together with the resulting slope (m) of the best-fit line. The lowest RMSE values among the two-parameter methods are displayed in bold for each aggregation period and group of sites considered. The single-parameter estimate (Equation 11) is bold-faced when it yields better estimates than the two-parameter methods (without PF_2).

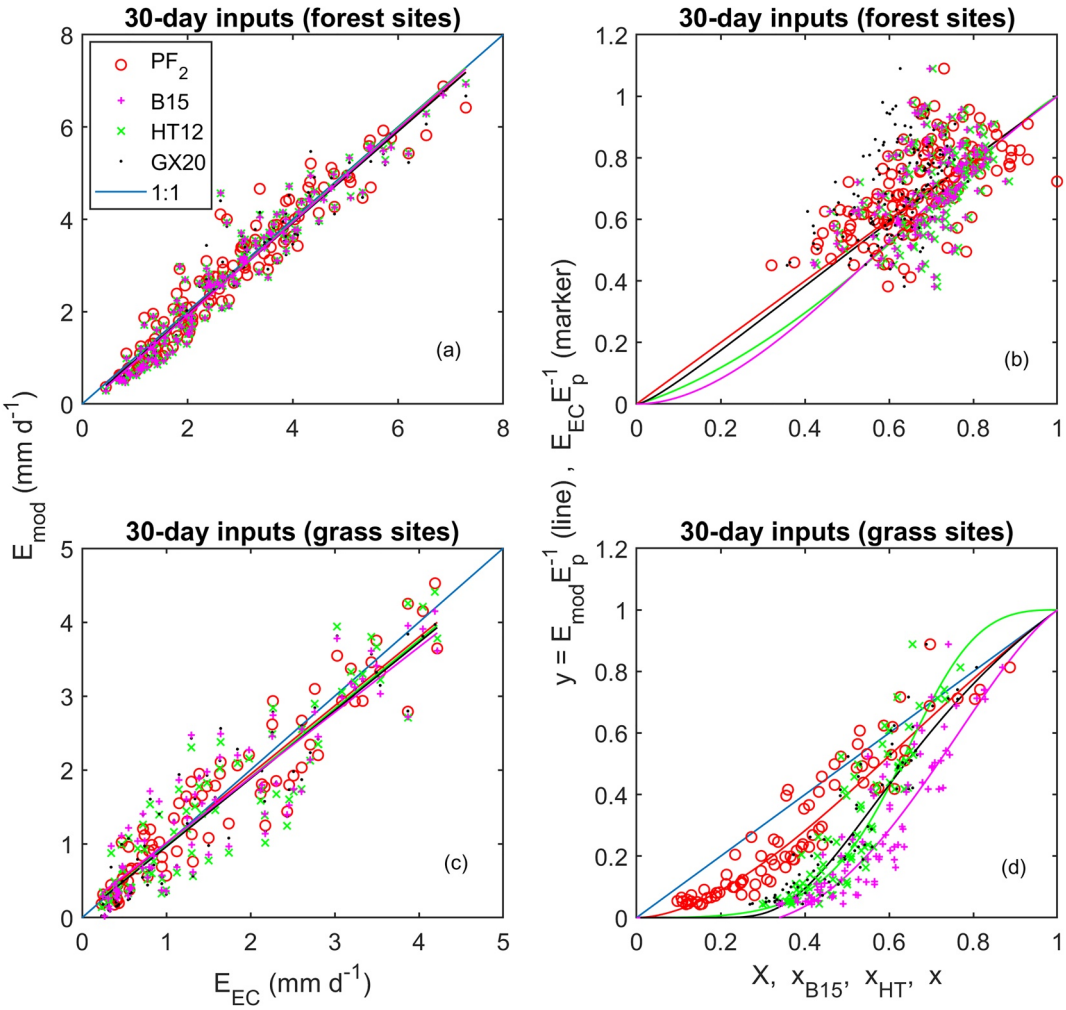

Figure 7. Regression plots of the modeled (E_{mod}) 30-day evaporation rates against eddy-covariance measurements (E_{EC}) at two forested (a) and two grass (c) sites of FLUXNET in Australia (see Figure 6 for locations) together with the least-squares-fitted straight lines. Graphical representation of the calibrated (see Table 3) nondimensional formulas (b), (d) listed in Table 2 plus that of PF_2, displayed with the nondimensional E_{EC} measurements. Color coding for the best-fit lines and the theoretical curves comes from the markers.

the latter is very sensitive to moisture changes in its *VPD* term due to the steep slope of the saturation vapor pressure curve at higher temperatures. A dropping E_p value will then boost both the wetness index, w_i, and the $E_w E_p^{-1}$ term of X and combined will increase its value by a larger degree than that of y, moving the measurement points in Figure 7d away from the 1:1 line for $0.2 < X < 0.45$. The measurement points however will follow the diminishing slope of PF_2 at extremely low X (<0.2) values (as seen in Figure 7d) and get closer to the 1:1 line again when large-scale horizontal moisture advection itself weakens as arid conditions probably spread spatially.

Note that the 1:1 line forms a theoretical upper limit to the measured nondimensional evaporation rates for B15 and GX21 only, as these models relate $E E_p^{-1}$ to $E_w E_p^{-1}$ with the $E \le E_w$ expectation. While such is the case mostly for the grass sites (Figure 7d), it is not so for the forested ones (Figure 7b), due to their improper scaling that produces x_{B15} and x (Table 2), respectively, instead of the thermodynamically backed one for X, first suggested by Szilagyi et al. (2017).

The relative importance of moisture admixing may change over the year, especially in areas with distinct wet and dry seasons, affecting the calibrated b value, such as clearly discernible at the monsoon-affected northern grassland site, east of the Gulf of Carpentaria in Figure 6. In the wet season (December-April) evaporation rates are typically high (Figure 8), advection effects are mild, reflected in a calibrated b value of 1.4. However, even during

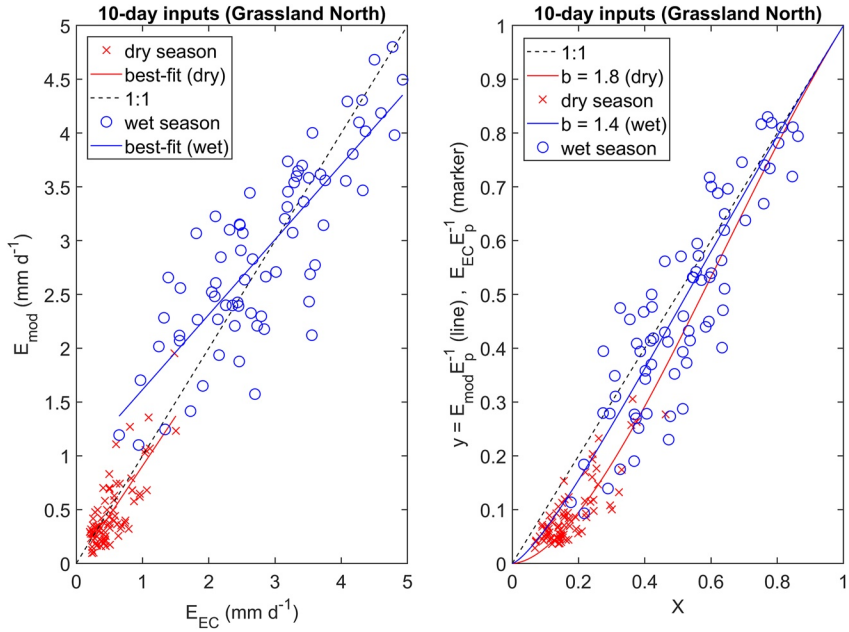

Figure 8. (a) Regression plot of the modeled (E_{mod}) 10-day evaporation rates against eddy-covariance measurements (E_{EC}) at the Grassland North FLUXNET site together with the least-squares-fitted straight lines separately for the wet- (December-April) and dry-season (June-October). (b) Graphical representation of PF_2, calibrated separately for the wet- and the dry-season, displayed with the nondimensional E_{EC} measurements. Color coding for the best-fit lines and the theoretical curves comes from the markers.

the wet season, the site may occasionally become moderately dry, with corresponding X values smaller than 0.4. During these events the relative importance of moisture transport from the Gulf or the Indian Ocean (Fig. S1 in Supporting Information S1) strengthens, resulting in an overestimation of the measured EC evaporation rates in Figure 8 (also causing the large deviation of the slope of the best-fit line from the 1:1 line). Note that for the same X values during the dry season (June–October), with a calibrated b value of 1.8, signifying relatively stronger moisture-advection effect from the Gulf (Fig. S1 in Supporting Information S1), PF_2 yields close to unbiased evaporation estimates. Note that the emphasis is on 'relative' in terms of moisture advection, since the same amount of extra moisture can result in larger evaporation reduction when the vapor pressure value is already low, as was demonstrated in Figure 5.

5. Testing the Power-Function (PF_2) Approach With Gridded Simplified Water-Balance Data

The PF_2 of Equation 13 is further tested across Australia for the spatial distribution of its b value, employing 0.25° monthly estimates of E_w, E_p, and E_p^{dry} calculated with ERA5 data from the global study of Ma et al. (2021), except that R_n now comes from the Global Land Data Assimilation System Version 2.1 (Beaudoing & Rodell, 2020) with a correction to match the climatological mean monthly values of the Clouds and the Earth's Radiant Energy System product (Kato et al., 2018). Similar to the FLUXNET data, no radiative corrections, such as detailed in Huwald et al. (2009) and possibly quite significant, were attempted for the air temperature values.

The monthly evaporation terms are aggregated to a 0.5° spatial resolution over the 2003–2012 time period together with the 0.25° precipitation values from the Global Precipitation Climatology Center (GPCC) Full Data Monthly Version 2018 (Schneider et al., 2018). Multiyear, simplified water-balance derived evaporation (E_{wb}) rates as precipitation (P) less runoff (Q) less change in water storage (ΔS) are calculated on a cell-by-cell basis by taking the arithmetic average of two monthly 0.5° gridded global runoff rates from the gauge-derived database of Ghiggi et al. (2019), and the synthesis of 11 land surface models by Hobeichi et al. (2019). The two sources of the runoff values are necessary due to the scarcity and uneven distribution of the monitoring watersheds (Fowler et al., 2021) across Australia large enough to accommodate the model cells. The Gravity Recovery and Climate Experiment (GRACE) (Tapley et al., 2004) data from the Jet Propulsion Laboratory Mascon RL06 Version

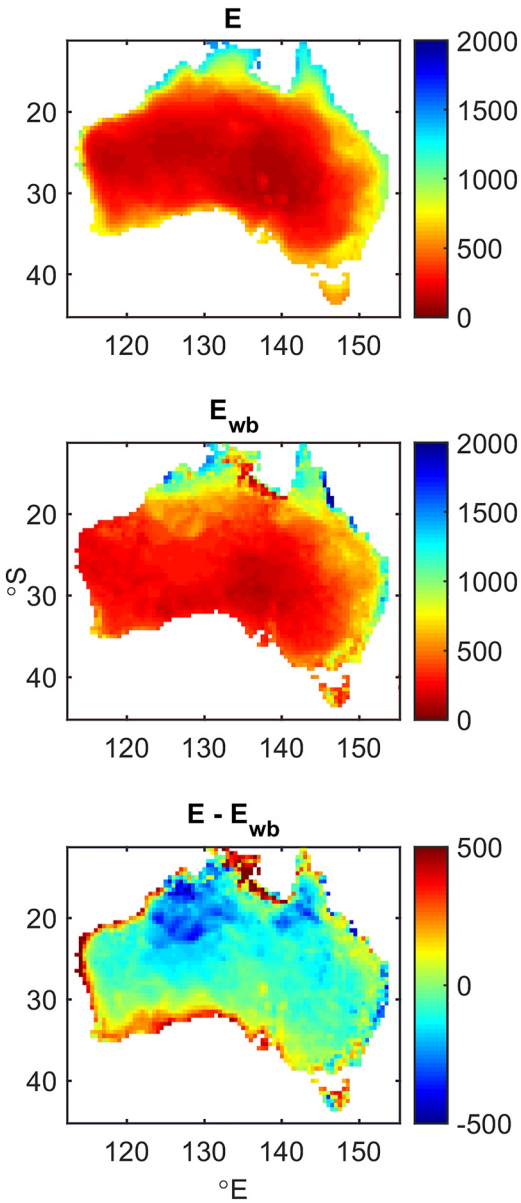

Figure 9. Spatial distribution of the 0.5° multiyear (2003–2012) mean annual evaporation (E) rates (mm yr^{-1}) across Australia by (a) Equation 11; (b) simplified water balance, E_{wb} (= $P - Q - \Delta S$), and; (c) their difference.

2.0 (Watkins et al., 2015) is used for deriving the annual ΔS values at 0.5° resolution, which are calculated as the difference in terrestrial water storage anomaly of successive Decembers.

The polynomial equation (Equation 11) without any calibration, estimates (Figure 9) the continent-wide (with Tasmania included) multiyear mean annual water-balance evaporation ($\langle E_{wb} \rangle$) rate of 457 mm yr^{-1} within 8%, that is, $\langle E \rangle$ = 424 mm yr^{-1}. The value of the PT-α in Equation 11 was set to 1.1 globally by Ma et al. (2021) via the method of Szilagyi et al. (2017), requiring no calibration, therefore no precipitation or runoff data, yet yields a local minimum in the root-mean-squared error (RMSE) of the multiyear cell-mean values of Australia within the $1.08 \leq \alpha \leq 1.14$ range tested (see Table A1 in the Appendix). Such a calibration-free setting of the PT-α value can only be performed for large-scale data sets ensuring the presence of permanently or at least periodically wet areas within their spatial domain.

The polynomial CR (Equation 11, $\alpha = 1.1$) without any parameter to account for differences in external moisture effects, overestimates the water-balance evaporation rates near the southern and western seashore where the prevailing winds (see Fig. S1 in Supporting Information S1) carry moisture laden air from the ocean to the land during a significant period of the year, thus largely decoupling the moisture content of the air from that of the underlying arid or semi-arid land surface. Naturally, the more arid the land, the stronger the overestimation that results from the elevated moisture content of the air. The strongest overestimation, however, occurs along the western side of the Gulf of Carpentaria in the north where the E_{wb} values are unusually low along a south-west to north-east patch. Otherwise, Equation 11 significantly underestimates the water-balance values in northern Australia characterized by a monsoonal precipitation (Fig. S2 in Supporting Information S1) regime (Sturman & Tapper, 1996), for reasons discussed below.

To study the effect of moisture advection spatially, the value of the parameter b in PF_2 (α = 1.1) is calibrated on a cell-by-cell basis by minimizing the absolute difference in the multiyear mean annual model-estimated and water-balance derived evaporation rates. Figure 10 displays the resulting spatial distribution of the calibrated values. As seen, the spatial pattern of the values strongly follows that of the estimation error in Figure 9: elevated values where the estimation error is positive and depressed ones where it is negative. This is to be expected, as the measurement points (E_{wb} or E_{EC}) are fixed in the nondimensional graph once the value of α is set within X. An overestimation (i.e., when the curve is above a given marker point in, e.g., Figure 7d) in PF_2 can only be corrected by moving the curve to the right which is achieved by increasing the value of b (Figure 4), and vice versa for an underestimation.

Naturally, the calibration yields model estimates very close to the 'observed' values (Figure 10) in each cell with only a low number of exceptions. The resulting continent-wide multiyear mean annual value of $\langle E \rangle$ = 450 mm yr^{-1} is indeed within 2% of the water-balance value (457 mm yr^{-1}) which thus also reduces the multiyear cell-mean RMSE value significantly (Table A1). Performance improvements in the corresponding continent-wide annual evaporation estimates are naturally less significant (Table A1) as estimation errors caused by a constant value of b tend to cancel each other when aggregated over a large region.

The histogram of the calibrated values of b is displayed in Figure 11 with a corresponding mean value of $\langle b \rangle$ = 1.96.

An interesting property of the histogram is that it is bimodal, with a secondary peak near b = 1. As discussed before, a unity value of b and a linear relationship between y and X (except in the vicinity of X = 0 where the

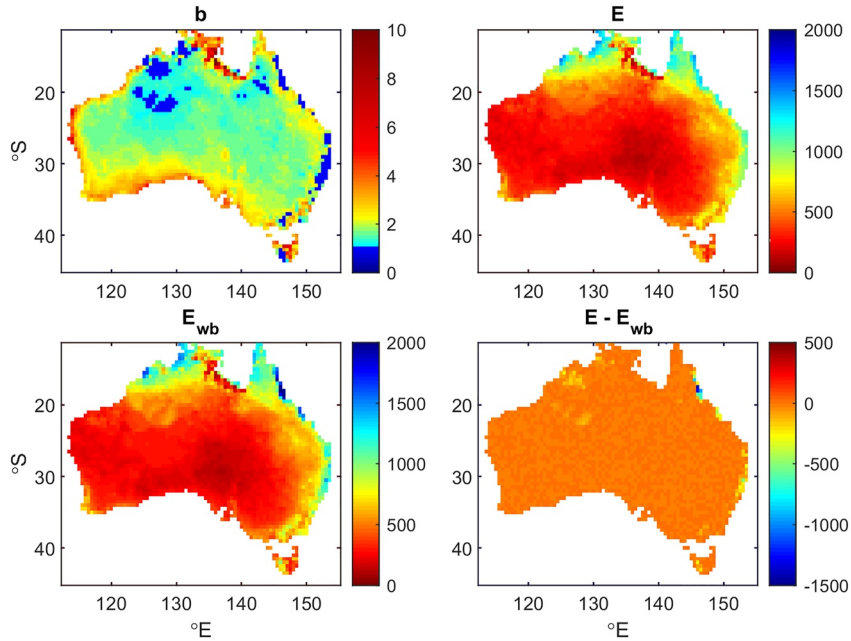

Figure 10. Spatial distribution of the (a) calibrated value of b in PF_2; (b) resulting multiyear (2003–2012) mean annual evaporation (E) rates (mm yr^{-1}) by PF_2; (c) simplified water-balance (E_{wb}) estimates (mm yr^{-1}) for comparison, and; (d) their difference.

slope must vanish due to the BCs in Equations 11 and 13) can be expected when external moisture influences over the region are negligible. Such conditions may most commonly exist if i) the environment itself remains humid throughout the year, and/or; ii) during its moderate drying (i.e., still remaining relatively humid) the prevailing wind arrives from areas of similar wetness. From the distribution of the calibrated b values in Figure 10, case i) must apply along parts of the eastern coast of Australia, within the Australian Alps, and the western part of Tasmania, while case ii) must generally be true for the monsoon region (Fig. S2 in Supporting Information S1) of northern Australia with the exception of the northern-most tip of Arnhem Land, west of the Gulf of Carpentaria where the E_{wb} values are most probably correct. This difference in the calibrated b values within the monsoon region is likely caused by differences in where the wind comes from during the dry season. As Fig. S1 in Supporting Information S1 attests, at the tip of Arnhem Land the wind always (summer and winter, i.e., within the wet and dry seasons) arrives from the nearby Indian Ocean or the Gulf, while it is not so for the rest of the monsoonal areas with calibrated values of b close to unity. During the dry season these latter areas receive air masses that emanate out of the most arid part of Australia (Fig. S1b in Supporting Information S1) bringing little moisture within, therefore external moisture effects remaining negligible throughout the year.

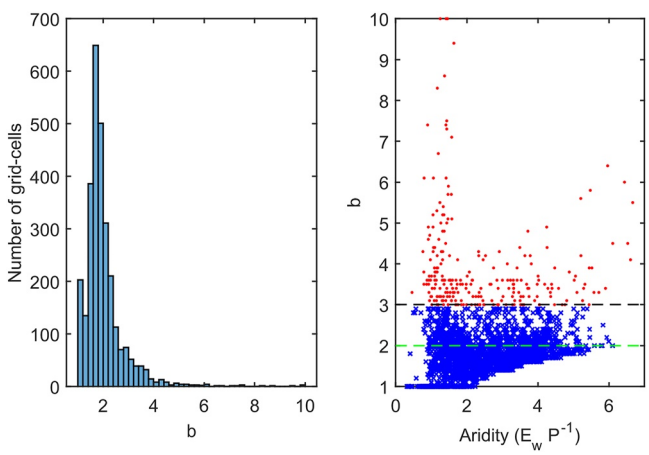

Figure 11. (a) Histogram of the b values obtained via a cell-by-cell calibration of PF_2 against the multiyear mean annual E_{wb} rate. (b) The calibrated b values plotted against the aridity index (ratio of the multiyear wet-environment evaporation rate, E_w, and precipitation), marked by red dots when $b \geq 3$.

As further seen in Figure 11, about 95% of the histogram values are less than three. In fact, $b \geq 3$ occurs predominantly along the dry southern and western seashore of Australia as a result of an overestimation of Equation 11 (Figure 9) due to the significant moisture transport from the ocean largely decoupling the moisture status of the air from its dry land surface, at least during a considerable period of the year. Similarly high values are found in eastern Tasmania downwind of the humid western part affected by topography-enhanced elevated rates of precipitation and thus humidity (Figure 10a) (The overestimation by Equation 11 along the western side of the Gulf of Carpentaria is most likely the consequence of the underestimated water-balance-derived values in Figure 10).

The calibrated b values when plotted against the aridity index, A_i ($= E_w P^{-1}$), of the cell in Figure 11, scatter significantly around the value of two in humid

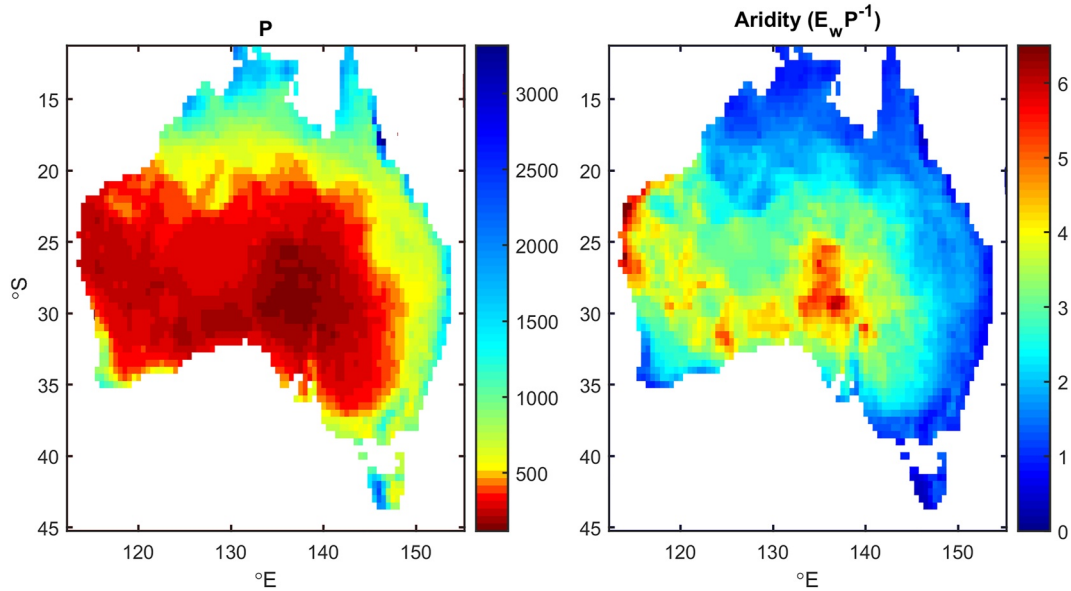

Figure 12. Spatial distribution of the multiyear (2003–2012) mean annual precipitation (P) rates (mm yr^{-1}) and the aridity index ($E_w P^{-1}$).

environments (i.e., A_i less than about 1.5, see also Figure 12), yet with a predominant single value of unity. The range of the b values decreases with aridity, as the minimum value b may drop to increases with aridity, with a well-defined sharp lower envelope for $A_i > 2$. This lower envelope stays unchanged (see Fig. S3 in Supporting Information S1) even when the cell-size is increased (and the corresponding scatter drops) to filter out the effect of cells near sudden discontinuities in surface wetness, predominantly cells close to the sea. It serves as further strong evidence that the value of b in PF_2 reflects the general influence external moisture import can exert on the land-atmosphere coupling of an area during wetting-drying cycles of the environment. The actual effect of this moisture import may depend on many factors such as distance and location (relative to the prevailing wind) to any sudden inhomogeneities in surface moisture, the degree of general inhomogeneity, average cluster size and range, spatial distribution and gradation, and so on, of the land in terms of soil, vegetation and therefore soil moisture properties, but also on the climate as well as on meteorological variables (mean, range, temporal variability, etc.), reflected in the sizable scatter of the points. All of these differences notwithstanding, aridity determines eventually (in the form of a sharp and steady lower envelope) the minimum (ensured) degree of influence one can expect from such moisture import on the resulting PF_2 curve. As any moisture import has a stronger upsetting potential the smaller the values to be disturbed are, the ensured influence increases with aridity (in the multiyear average sense) which translates to PF_2 curves of increasing b ($1 \leq b \leq 2$) values.

Finally, the overall consistency of the calibrated b values (with a correlation coefficient of 0.74 in Table A1) between the local and regional scale can be most vividly seen when one compares the gridded-data-derived values with those obtained from FLUXNET measurements, both listed in Table 4. Only at the southernmost site (Wallaby Creek) is there a significant difference in the two calibrated values, where the large-scale horizontal moisture transport likely from the nearby (about 70 km away) ocean is felt stronger by the grid cell covering not only the forest but other land-covers (ESA, 2009) expected to be drier than the forested land (Figure 13). It is generally true from Table 4 that grid data is more sensitive to large-scale moisture transport than local ones in humid settings, expressed in somewhat larger grid-derived b values for FLUXNET sites of $b = 1$.

Table 4 also indicates that the value of b and its spatial behavior with gridded data are not influenced or constrained by a correctly set constant value (i.e., $\alpha = 1.1$) of the PT-α since with FLUXNET data both PT-α and b are simultaneously calibrated yet yield similar values of b as the gridded data. A systematic increase in the correctly set constant value of the PT-α—in order to bring it closer to the average PT-α value of 1.14 with the 30-day aggregated FLUXNET data—results in growing differences in the two calibrated values of b (reflected by sharply dropping values of the linear correlation coefficient, R_{bb}, in Table A1) at the FLUXNET sites. But this is

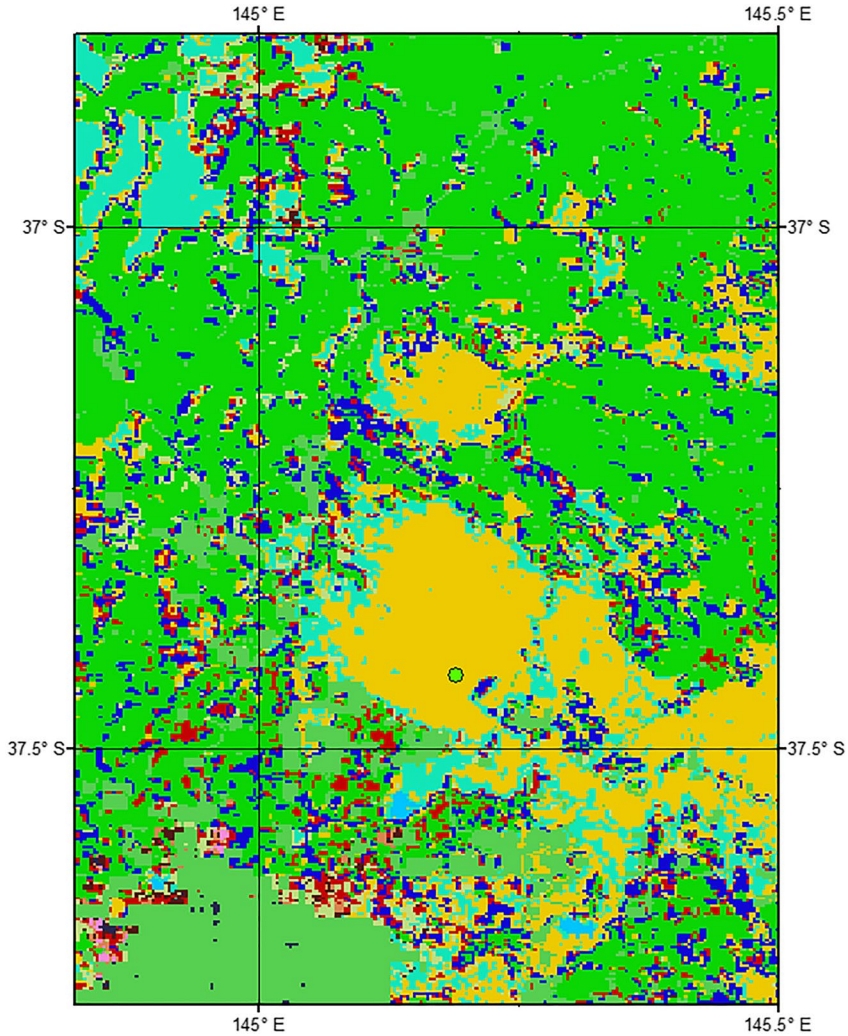

Figure 13. Location (circle) of the evergreen broadleaf forest (West) eddy-covariance site (Wallaby Creek) of Table 4 (last row) within the 0.5° (between 37°–37.5°S and 145°–145.5°E) grid-cell covering it. The predominant land-cover category according to the United Nations Land Cover Classification System is 'rainfed croplands' in green color (ESA, 2009). The forested areas are displayed in light brown. The cell is about 55 km in size.

again to be expected, as Szilagyi et al. (2017) pointed out that the optimal value of the PT-α is mainly influenced by the spatial and temporal resolution of the input data itself.

6. Summary and Conclusions

The three-parameter power-function (PF_3) extension, Equation 12, of the nondimensional polynomial CR of Equation 11, the latter derived from thermodynamic considerations, introduces two parameters, a and b, additional to the PT-α in Equation 11. By setting $a = 2$, the resulting PF_2 equation (Equation 13) can reproduce the polynomial version, Equation 11, via the $b = 2$ choice, and the linear CR of Equation 10, provided $b = 1$.

Calibration of the PT-α and b with FLUXNET data results in a two-parameter CR version (PF_2) that excels among three additional two-parameter CR models in its estimation of the daily, 5- and 30-day aggregated latent heat fluxes. The calibrated value of b becomes unity with 30-day aggregated inputs at four FLUXNET sites, two of them situated in a wet climate with mean annual precipitation in excess of 1500 mm, while the other two sites are located in evergreen broadleaf forests enjoying about 700 mm of rain annually. At the driest, open shrubland site, the calibrated value of b becomes two, while at the remaining two sites somewhat smaller than that.

Table 4
Calibrated Values of b in PF_2 From the (i) FLUXNET 30-Day Aggregated Measurements, and (ii) Monthly 0.5° Data For the Grid-Cell (2003–2012) Covering the Site

FLUXNET sites in Figure 6 (north to south)	FLUXNET site latitude, longitude	FLUXNET *b*	Grid-cell *b*
Woody savanna	12.50° S, 131.15° E	1	1.4
Permanent wetland	12.54° S, 131.31° E	1	1.4
Grassland (North)	17.15° S, 133.35° E	1.7	1.6
Open shrubland	22.29° S, 133.64° E	2	1.9
Evergreen broadleaf forest (East)	35.66° S, 148.15° E	1	1.5
Grassland (South)	36.65° S, 145.58° E	1.9	2.1
Evergreen broadleaf forest (West)	37.43° S, 145.19° E	1	1.8

With the help of gridded precipitation and runoff data, the calibration of b in PF_2 was repeated on a cell-by-cell basis with 0.5° gridded monthly inputs to Equation 13 across Australia over a whole decade with a spatially and temporally constant PT-α value of 1.1, set by the method of Szilagyi et al. (2017). In the cells that cover the FLUXNET sites the gridded-data-derived b values generally follow those obtained by eddy-covariance data. Only at one forest site is there a larger difference where the predominant land cover of the 0.5° cell overlying the site is rainfed cropland which probably explains the difference in the calibrated b values, that is, unity for the forested site and 1.8 for the cell.

The cell-by-cell-calibrated b values follow a bimodal distribution (mean of 1.96) with a primary mode around two and a secondary one near unity. The spatial distribution of the b values confirms and explains findings by Crago and Qualls (2018), who employed the same FLUXNET sites, of why a linear nondimensional CR relationship (corresponding to $b = 1$ in PF_2) yields the best estimate for certain locations.

While Szilagyi (2021) in his thermodynamics-based derivation of Equation 11 correctly deduced that a vanishing slope of the corresponding curve near $X = 0$ can only occur when the difference in e_s and e_a also vanishes, he failed to identify the process that can produce it in general. The spatial distribution of the calibrated b values in Figure 10, plus the site-by-site calibration results, help to find it. That process is the incorporation (delivered via horizontal advection and/or vertical entrainment of free-tropospheric air by the day-time growing convective boundary layer) and turbulent mixing of external moisture into the air overlying the drying area which can clearly produce a vertically near-constant humidity gradient and thus a vanishing difference in the e_s and e_a variables at small X values. This (horizontal and/or vertical) moisture transport then leads to $dy/dX \to 0$ as $X \to 0$ and thus produces Equation 11. Further exploration is required to explain why this polynomial solution acts as an attractor to the more flexible power-function expansion of PF_2 (yielding a mean b value of 1.96), considering that the polynomial (just like the PF) approach is just a mathematical convenience (satisfying the four BCs) without any physically based differential equation yet defined behind it. The linear solution of Equation 10 as the other attractor for the PF curves, in contrast, results from purely thermodynamic reasoning.

When the effect of external moisture is negligible due to minimal spatial differences in moisture conditions between the study region and its wider environment (possible in large parts of the monsoon areas of Australia, along parts of its eastern shore, and in western Tasmania) or when the incorporated air is drier than the air overlying the region, typical of humid and sub-humid conditions, for example, in the winter months along the eastern-most shore of Australia (Fig. S1 in Supporting Information S1), the constant relative speed conjecture of the state coordinates, (e_a, T_a) versus (e_s, T_s) along the air and surface isenthalps (Figure 1), first postulated by Szilagyi (2021), seems to be validated by the calibrated b values of unity across these regions of Australia, and thus reproduce the linear CR version of Equation 10. Naturally, the preservation of a constant relative speed between the two isenthalps' state coordinates cannot be expected to exist in a strict sense at all times, due to unavoidable changes in Q_n, air pressure, and/or wind conditions during the day, but it may happen as a mean behavior over the averaging period (typically from a day to a month), the more so as temporal averaging increases, as seen in Table 3 with the FLUXNET data and also corroborated by Crago et al. (2022).

Equation 13 (PF_2) may be preferable over the existing single-parameter (and calibration-free when applied with gridded data of a large domain) polynomial approach of Equation 11, due to its built-in flexibility when

calibration is made possible by available measured (e.g., eddy-covariance) or water-balance based estimates of land evaporation and/or the possibility exists that a linear CR approach (i.e., when $b = 1$ in Equation 13) yields a better estimate than a polynomial one.

An additional useful property of PF_2 may be that after proper calibration, it can be applied in regions near sudden jumps in surface moisture conditions, such as seashores, at least as long as the land-atmosphere coupling is not severely disrupted and overwhelmed by the imported moisture.

Appendix A

Table A1
Performance Measures for the Evaporation Estimates of Equation 11 (i.e., Equation 13 With b = 2) and 13 Against the Simplified Water-Balance-Derived (i) Multiyear Mean Annual Cell Evaporation Rates, and (ii) Continent-Wide Annual Evaporation Rates

		Multiyear mean annual cell evaporation			Continent-wide annual evaporation		
Parameter α	Parameter b	$\langle\varepsilon\rangle$ (mm yr^{-1})	RMSE (mm yr^{-1})	R_{bb} (−)	$\lvert\varepsilon\rvert$ (mm yr^{-1})	RMSE (mm yr^{-1})	R (−)
$\alpha = 1.08$	$b = 2$	−51.11	179.83		58.38	65.76	0.91
	$\langle b\rangle = 1.88$	−9.06	60.76	0.76	35.89	41.5	0.9
$\alpha = 1.09$	$b = 2$	−42.18	179.09		51.88	58.67	0.91
	$\langle b\rangle = 1.92$	−8.16	58.69	0.71	35.22	40.73	0.9
$\alpha = 1.1$	$b = 2$	−33.14	178.96[a]		46.31	52.09	0.91
	$\langle b\rangle = 1.96$	−7.31	56.73	0.74[a]	34.56	39.97	0.9
$\alpha = 1.11$	$b = 2$	−23.99	179.48		40.69	46.3	0.91
	$\langle b\rangle = 2$	−6.86	54.84	0.58	34.06	39.31	0.9
$\alpha = 1.12$	$b = 2$	−14.74	180.67		36.73	41.71	0.91
	$\langle b\rangle = 2.05$	−5.89	53.05	0.44	33.34	38.55	0.9
$\alpha = 1.13$	$b = 2$	−5.38	182.52		32.78	38.83	0.91
	$\langle b\rangle = 2.09$	−5.5	51.41	0.28	32.82	37.9	0.9
$\alpha = 1.14$	$b = 2$	4.08	185.04		29.62	38.12	0.91
	$\langle b\rangle = 2.14$	−5.28	49.87	0.19	32.38	37.29	0.9

Note. $\langle b\rangle$: cell-wide average of the calibrated b values; $\langle\varepsilon\rangle$: cell-wide average of the errors in the multiyear cell-mean values; $\lvert\varepsilon\rvert$: mean absolute error in the continent-wide annual values; RMSE: root-mean-squared-error of the multiyear cell-mean values or the continent-wide annual values; R: correlation coefficient for the continent-wide annual values. R_{bb}: correlation coefficient between FLUXNET-data derived b values in Table 4 and the E_{wb}-calibrated b values for the cell covering the site, under the prescribed α value in this Table.

[a]Local minimum or maximum within the range of α applied (i.e., [1.08–1.14]).

Data Availability Statement

All data used in this study are publicly available from the following sites. Daily FLUXNET values (http://fluxnet.fluxdata.org/sites/site-list-and-pages/); GPCC precipitation (https://opendata.dwd.de/climate_environment/GPCC/html/fulldata-monthly_v2018_doi_download.html); runoff data (https://doi.org/10.6084/m9.figshare.9228176, https://geonetwork.nci.org.au/geonetwork/srv/eng/catalog.search#/metadata/f9617_9854_8096_5291); ERA5 data (https://www.ecmwf.int/en/forecasts/datasets/reanalysis-datasets/era5); GLDAS V2.1 R_n (https://disc.gsfc.nasa.gov/datasets/GLDAS_NOAH025_M_2.1/summary); GRACE (https://grace.jpl.nasa.gov/data/get-data/jpl_global_mascons/); ESA land cover (https://databasin.org/datasets/a08ff893bed248d2b6add102a3aa0101/).

Acknowledgments
Support provided by the Ministry of Innovation and Technology of Hungary from the National Research, Development and Innovation Fund, financed under the TKP2021 funding scheme (project BME-NVA-02); the National Natural Science Foundation of China (project 42271029), and by; the USDA NIFA grant IDA01584 is kindly acknowledged. The authors are grateful for the constructive comments of all three anonymous reviewers leading to important changes in the original text.

References

Andreas, E. L., Jordan, R. E., Mahrt, L., & Vickers, D. (2013). Estimating the Bowen ratio over the open and ice-covered ocean. *Journal of Geophysical Research: Oceans*, *118*(9), 4334–4345. https://doi.org/10.1002/jgrc.20295

Assouline, S., Tyler, S. W., Tanny, J., Cohen, S., Bou-Zeid, E., Parlange, M. B., & Katul, G. G. (2008). Evaporation from three water bodies of different sizes and climates: Measurements and scaling analysis. *Advances in Water Resources*, *31*(1), 160–172. https://doi.org/10.1016/j.advwatres.2007.07.003

Beaudoing, H., & Rodell, M. (2020). *GLDAS Noah land surface model L4 monthly 0.25 × 0.25 degree V2.1. Greenbelt, MD*. USA Goddard Earth Sciences Data and Information Services Center (GES DISC). https://doi.org/10.5067/SXAVCZFAQLNO

Bouchet, R. (1963). Evapotranspiration reelle et potentielle, signification climatique. *International Association of Hydrological Sciences Publication*, *62*, 134–142.

Brutsaert, W. (1982). *Evaporation into the atmosphere: Theory, history, and applications*. D. Reidel. https://doi.org/10.1007/978-94-017-1497-6

Brutsaert, W. (2015). A generalized complementary principle with physical constraints for land-surface evaporation. *Water Resources Research*, *51*(10), 8087–8093. https://doi.org/10.1002/2015WR017720

Brutsaert, W., Cheng, L., & Zhang, L. (2020). Spatial distribution of global landscape evaporation in the early twenty-first century by means of a generalized complementary approach. *Journal of Hydrometeorology*, *21*(2), 287–298. https://doi.org/10.1175/jhm-d-19-0208.1

Brutsaert, W., & Parlange, M. B. (1998). Hydrologic cycle explains the evaporation paradox. *Nature*, *396*(6706), 30. https://doi.org/10.1038/23845

Brutsaert, W., & Stricker, H. (1979). An advection-aridity approach to estimate actual regional evapotranspiration. *Water Resources Research*, *15*(2), 443–450. https://doi.org/10.1029/wr015i002p00443

Crago, R., & Qualls, R. (2018). Evaluation of the generalized and rescaled complementary relationships. *Water Resources Research*, *54*(10), 8086–8102. https://doi.org/10.1029/2018wr023401

Crago, R., & Qualls, R. (2021). A graphical interpretation of the rescaled complementary relationship for evapotranspiration. *Water Resources Research*, *57*(8). https://doi.org/10.1029/2020wr028299

Crago, R., Qualls, R., & Szilagyi, J. (2022). Complementary relationship for evaporation: Performance at different spatial and temporal scales, Journal of Hydrology, *608*(4), 127575.

deBruin, H. A. R. (1982). A model for the Priestley-Taylor parameter α. *Journal of Climate and Applied Meteorology*, *22*, 572–578. https://doi.org/10.1175/1520-0450(1983)022<0572:amftpt>2.0.co;2

Eichinger, W. E., Parlange, M. B., & Stricker, H. (1996). On the concept of equilibrium evaporation and the value of the Priestley-Taylor coefficient. *Water Resources Research*, *32*(1), 161–164. https://doi.org/10.1029/95wr02920

European Space Agency (ESA). (2009). GlobCover 2009. Retrieved from https://databasin.org/datasets/a08ff893bed248d2b6add102a3aa0101/

Fowler, K. J. A., Acharya, S. C., Addor, N., Chou, C., & Peel, M. C. (2021). CAMELS-AUS: Hydrometeorological time series and landscape attributes for 222 catchments in Australia. *Earth System Science Data*, *13*(8), 3847–3867. https://doi.org/10.5194/essd-13-3847-2021

Gao, B., & Xu, X. (2021). Derivation of an exponential complementary function with physical constraints for land surface evaporation estimation. *Journal of Hydrology*, *593*, 125623. https://doi.org/10.1016/j.jhydrol.2020.125623

Ghiggi, G., Humphrey, V., Seneviratne, S. I., & Gudmundsson, L. (2019). GRUN: An observations-based global gridded runoff dataset from 1902 to 2014. *Earth System Science Data*, *11*(4), 1655–1674. https://doi.org/10.5194/essd-11-1655-2019

Han, S., Hu, H., & Tian, F. (2012). A nonlinear function approach for the normalized complementary relationship evaporation model. *Hydrological Processes*, *26*(26), 3973–3981. https://doi.org/10.1002/hyp.8414

Han, S., & Tian, F. (2018). Derivation of a sigmoid generalized complementary function for evaporation with physical constraints. *Water Resources Research*, *54*(7), 5050–5068. https://doi.org/10.1029/2017WR021755

Han, S., & Tian, F. (2020). A review of the complementary principle of evaporation: From original linear relationship to generalized nonlinear functions. *Hydrology and Earth System Sciences*, *24*(5), 2269–2285. https://doi.org/10.5194/hess-24-2269-2020

Hobeichi, S., Abramowitz, G., Evans, J., & Beck, H. E. (2019). Linear optimal runoff aggregate (LORA): A global gridded synthesis runoff product. *Hydrology and Earth System Sciences*, *23*(2), 851–870. https://doi.org/10.5194/hess-23-851-2019

Huwald, H., Higgins, C. W., Boldi, M.-O., Bou-Zeid, E., Lehning, M., & Parlange, M. B. (2009). Albedo effect on radiative errors in air temperature measurements. *Water Resources Research*, *45*(8), W08431. https://doi.org/10.1029/2008WR007600

Kato, S., Rose, F. G., Rutan, D. A., Thorsen, T. J., Loeb, N. G., Doelling, D. R., et al. (2018). Surface irradiances of edition 4.0 clouds and the Earth's radiant energy system (CERES) energy balanced and filled (EBAF) data product. *Journal of Climate*, *31*(11), 4501–4527. https://doi.org/10.1175/jcli-d-17-0523.1

Katul, G. G., & Parlange, M. B. (1992). A Penman-Brutsaert model for wet surface evaporation. *Water Resources Research*, *28*(1), 121–126. https://doi.org/10.1029/91wr02324

Kim, D., Lee, W.-S., Kim, S. T., & Chun, J. A. (2019). Historical drought assessment over the contiguous United States using the generalized complementary principle of evapotranspiration. *Water Resources Research*, *55*(7), 6244–6267. https://doi.org/10.1029/2019WR024991

Laikhtman, D. L. (1964). *Physics of the boundary layer of the atmosphere*. Sivan Press.

Lhomme, J. P. (1997). A theoretical basis for the Priestley-Taylor coefficient. *Boundary-Layer Meteorology*, *82*(2), 179–191. https://doi.org/10.1023/A:1000281114105

Ma, N., & Szilagyi, J. (2019). The CR of evaporation: A calibration-free diagnostic and benchmarking tool for large-scale terrestrial evapotranspiration modeling. *Water Resources Research*, *55*(8), 7246–7274. https://doi.org/10.1029/2019WR024867

Ma, N., Szilagyi, J., & Jozsa, J. (2020). Benchmarking large-scale evapotranspiration estimates: A perspective from a calibration-free complementary relationship approach and FLUXCOM. *Journal of Hydrology*, *590*, 125221. https://doi.org/10.1016/j.jhydrol.2020.125221

Ma, N., Szilagyi, J., & Zhang, Y. (2021). Calibration-free complementary relationship estimates terrestrial evapotranspiration globally. *Water Resources Research*, *57*(9), e2021WR029691. https://doi.org/10.1029/2021WR029691

Ma, N., Szilagyi, J., Zhang, Y., & Liu, W. (2019). Complementary-relationship-based modeling of terrestrial evapotranspiration across China during 1982-2012: Validations and spatiotemporal analyses. *Journal of Geophysical Research-Atmospheres*, *124*(8), 2018JD029850. https://doi.org/10.1029/2018jd029850

McNaughton, K. G. (1976). Evaporation and advection. *Quarterly Journal of the Royal Meteorological Society*, *102*(431), 181–191. https://doi.org/10.1002/qj.49710243115

McNaughton, K. G., & Spriggs, T. W. (1989). An evaluation of the Priestley and Taylor equation and the complementary relationship using results from a mixed-layer model of the convective boundary layer. *Estimation of Areal Evapotranspiration. IAHS Publications*, *177*, 89–104.

Monteith, J. L. (1981). Evaporation and surface temperature: Evaporation and surface temperature. *Quarterly Journal of the Royal Meteorological Society*, *107*(451), 1–27. https://doi.org/10.1002/qj.49710745102

Morton, F. I. (1983). Operational estimates of areal evapotranspiration and their significance to the science and practice of hydrology. *Journal of Hydrology*, *66*(1–4), 1–76. https://doi.org/10.1016/0022-1694(83)90177-4

Parlange, M. B., & Katul, G. G. (1992). An advection-aridity evaporation model. *Water Resources Research*, *28*(1), 127–132. https://doi.org/10.1029/91wr02482

Pastorello, G., Trotta, C., Canfora, E., Chu, H., Christianson, D., Cheah, Y. W., et al. (2020). The FLUXNET2015 dataset and the ONEFlux processing pipeline for eddy covariance data. *Scientific Data*, *7*(1), 225. https://doi.org/10.1038/s41597-020-0534-3

Penman, H. L. (1948). Natural evaporation from open water, bare soil and grass. *Proceedings of the Royal Society A: Mathematics, Physics and Engineering Sciences*, *193*, 120–145. https://doi.org/10.1098/rspa.1948.0037

Priestley, C. H. B., & Taylor, R. J. (1972). On the assessment of surface heat flux and evaporation using large-scale parameters. *Monthly Weather Review*, *100*(2), 81–92. https://doi.org/10.1175/1520-0493(1972)100<0081:otaosh>2.3.co;2

Qualls, R. J., & Crago, R. D. (2020). Graphical interpretation of wet surface evaporation equations. *Water Resources Research*, *56*(10), e2019WR026766. https://doi.org/10.1029/2019wr026766

Schneider, U., Becker, A., Finger, P., Meyer-Christoffer, A., & Ziese, M. (2018). GPCC Full data monthly product version 2018 at 0.25°: Monthly land-surface precipitation from rain-gauges built on GTS-based and historical data. https://doi.org/10.5676/DWD_GPCC/FD_M_V2018_025

Stull, R. B. (2000). *Meteorology for Scientists and Engineers*. Brooks/Cole.

Sturman, A., & Tapper, N. (1996). *The weather and climate of Australia and New Zealand*. Oxford University Press.

Szilagyi, J. (2014). Temperature corrections in the Priestley-Taylor equation of evaporation. *Journal of Hydrology*, *519*, 455–464. https://doi.org/10.1016/j.jhydrol.2014.07.040

Szilagyi, J. (2021). On the thermodynamic foundations of the complementary relationship of evaporation. *Journal of Hydrology*, *593*, 125916. https://doi.org/10.1016/j.jhydrol.2020.125916

Szilagyi, J., Crago, R., & Qualls, R. (2017). A calibration-free formulation of the complementary relationship of evaporation for continental-scale hydrology. *Journal of Geophysical Research-Atmospheres*, *122*(1), 264–278. https://doi.org/10.1002/2016JD025611

Szilagyi, J., & Jozsa, J. (2008). New findings about the complementary relationship-based evaporation estimation methods. *Journal of Hydrology*, *354*(1–4), 171–186. https://doi.org/10.1016/j.jhydrol.2008.03.008

Szilagyi, J., Parlange, M. B., & Katul, G. G. (2014). Assessment of the Priestley-Taylor parameter value from ERA-Interim global reanalysis data. *Journal of Hydrology and Environmental Research*, *2*(1), 1–7.

Tapley, B. D., Bettadpur, S., Ries, J. C., Thompson, P. F., & Watkins, M. M. (2004). GRACE measurements of mass variability in the Earth system. *Science*, *305*(5683), 503–505. https://doi.org/10.1126/science.1099192

Turbiner, A. (1992). On polynomial solutions of differential equations. *Journal of Mathematical Physics*, *33*(12), 3989–3993. https://doi.org/10.1063/1.529848

Twine, T. E., Kustas, W. P., Norman, J. M., Cook, D. R., Houser, P. R., Meyers, T. P., et al. (2000). Correcting eddy-covariance flux underestimates over a grassland. *Agricultural and Forest Meteorology*, *103*(3), 279–300. https://doi.org/10.1016/S0168-1923(00)00123-4

Watkins, M. M., Wiese, D. N., Yuan, D., Boening, C., & Landerer, F. W. (2015). Improved methods for observing Earth's time variable mass distribution with GRACE using spherical cap mascons. *Journal of Geophysical Research: Solid Earth*, *120*(4), 2648–2671. https://doi.org/10.1002/2014JB011547